

The scattering of sound waves by a vortex: numerical simulations and analytical solutions

By **TIM COLONIUS, SANJIVA K. LELE† AND PARVIZ MOIN‡**
Department of Mechanical Engineering, Stanford University, Stanford, CA 94305, USA

(Received 4 July 1992 and in revised form 13 August 1993)

The scattering of plane sound waves by a vortex is investigated by solving the compressible Navier–Stokes equations numerically, and analytically with asymptotic expansions. Numerical errors associated with discretization and boundary conditions are made small by using high-order-accurate spatial differentiation and time marching schemes along with accurate non-reflecting boundary conditions. The accuracy of computations of flow fields with acoustic waves of amplitude five orders of magnitude smaller than the hydrodynamic fluctuations is directly verified. The properties of the scattered field are examined in detail. The results reveal inadequacies in previous vortex scattering theories when the circulation of the vortex is non-zero and refraction by the slowly decaying vortex flow field is important. Approximate analytical solutions that account for the refraction effect are developed and found to be in good agreement with the computations and experiments.

1. Introduction

The prediction of the sound produced by turbulent flow requires a detailed knowledge of acoustic source terms. Direct computation of both the acoustic sources and far-field sound using the unsteady Navier–Stokes equations allows direct validation of aeroacoustic theories. In a recent review by Crighton (1988), the difficulties involved in direct computations of aeroacoustic fields are discussed. These include: the large extent of the acoustic field compared with the flow field; the small energy of the acoustic field compared to the flow field; and the possibility that numerical discretization may introduce a significant sound source due to the acoustic inefficiency of low-Mach-number flows. In order to address these difficulties, Crighton proposed that direct computations be performed on elementary model aeroacoustic problems whose physics are well understood. For this reason, and to validate our numerical scheme for direct computation of aeroacoustic problems, we investigate the scattering of sound waves by a compressible viscous vortex. This problem has received significant attention, and thus provides a large database of theory, numerics and experiment with which detailed comparisons may be made. Yet there is significant disagreement amongst the various theories, which has not yet been fully rectified. Therefore, the purpose of the current work is twofold: to validate our numerical scheme for direct computation of aeroacoustic problems using the unsteady Navier–Stokes equations, and to investigate the scattering of sound waves by a compressible viscous vortex.

† Also with Department of Aeronautics and Astronautics, Stanford University.

‡ Also with NASA-Ames Research Center.

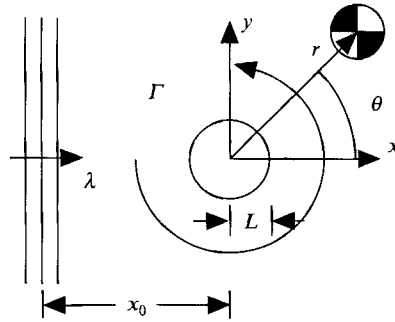


FIGURE 1. Schematic diagram of flow configuration.

Direct Navier–Stokes computations of both laminar and turbulent hydrodynamic fields have been performed for some time. However, little effort has been made to resolve the acoustic waves whose energy is many orders of magnitude smaller than the hydrodynamic field. In order to accurately resolve these small perturbations to the hydrodynamic fields, high-order-accurate numerical differentiation and time marching schemes are necessary (Colonius, Lele & Moin 1991*a*, 1992). Furthermore, aeroacoustic problems are typically defined on an infinite or semi-infinite domain, and the numerical solution of the discrete equations therefore requires truncation of the infinite domain, and the imposition of ‘artificial’ numerical boundary conditions at the edges of the computational domain. These artificial boundaries must in general not only be non-reflecting for acoustic waves, but must also allow inflow and outflow of the hydrodynamic mean flow and the passage of hydrodynamic disturbances at outflow boundaries. Boundary conditions sufficiently accurate for aeroacoustic computations have recently been developed and applied to a variety of test problems (Colonius *et al.* 1992); these boundary conditions are utilized in the present computations.

The scattering of sound waves by vortices is of interest in the prediction of the scattering of sound waves by turbulent shear flows where large-scale orderly vortical structures can dominate the flow. It has been proposed that the scattering of waves by the shear layer may be investigated by the simpler problem of the interaction of an incident wave with an isolated vortex (Candel 1979). Vortex scattering is also of interest in the detection and ranging of the trailing vortices of large transport aircraft (Ferziger 1974).

Figure 1 shows a schematic drawing of the flow configuration. A two-dimensional vortex is irradiated with sound waves, which are assumed to be planar at a distance $-x_0$ from the vortex centre. The waves propagate in the $+x$ -direction. The scattered field depends on the wavelength, λ , of the incident waves, and the profiles of velocity, density and pressure in the vortex. In general, two types of analysis are performed. In the limit where the wavelength of the incident sound is very much smaller than a characteristic size of the vortex, high-frequency ray-tracing techniques are used (e.g. Georges 1972). In the opposite case, where the wavelength of the incident sound is much larger than the characteristic lengthscale, then the Born approximation or low-frequency approach is used (Müller & Matschat 1959; Ferziger 1974; O’Shea 1975; Howe 1975; Yates 1978; Candel 1979). Note that the Born approximation is sometimes referred to as the first scattering approximation in the literature.

In applying the high- or low-frequency approximations to the scattering problem, the core size of the viscous vortex, L , has typically been assumed to be the characteristic

lengthscale. However, another lengthscale can be formed using the total circulation of the vortex, $\Gamma = \int \Omega \, dA$ (where Ω is the single component of the vorticity in the flow and the integration is performed over the infinite plane; hereafter the word circulation will always refer to the total circulation), and the sound speed far from the vortex, a_∞ . When the total circulation of the vortex is non-zero, then the tangential velocity field decays like $\Gamma/(2\pi r)$ for large r , where r is the distance away from the vortex centre. This slowly decaying velocity field causes refraction of the incident waves and therefore the lengthscale Γ/a_∞ controls the amount of refraction away from the vortex core.

The two lengthscales are related by the Mach number, M , of the vortex, defined as the maximum vortex velocity relative to the sound speed at infinity, a_∞ ,

$$M = \beta \frac{\Gamma}{2\pi L a_\infty}, \quad (1)$$

where β is a numerical constant which depends on the specific distribution of tangential velocity in the core of the vortex.

In the analyses mentioned above the refraction effect is often neglected. In the acoustic analogy analysis of Howe (1975), where the refraction is neglected, a scattered field which decays as $r^{-\frac{1}{2}}$ away from the vortex core is obtained. (For compact scatterers, one expects a $r^{-\frac{1}{2}}$ decay since the free-space Green's function for the Helmholtz operator decays as $r^{-\frac{1}{2}}$ in the far field.) A similar acoustic analogy analysis by Yates (1978) indicated that the dipole directivity pattern computed by Howe was incorrect, and that the correct scattered field directivity is quadrupole. However, when the refraction effect is included, the scattering amplitude was determined by both O'Shea (1975) and Yates (1978) to be infinite in the forward scattering direction. This was interpreted by O'Shea (1975) to mean that the scattering effect from the slow r^{-1} velocity decay cannot be predicted in the Born approximation, and that scattering and refraction should be distinguished and treated separately.

Müller & Matschat (1959) considered a point vortex, but introduced inner and outer cut-off radii outside which the tangential velocity is set to zero. By expanding the linearized Euler equations for small values of the parameter

$$\epsilon = \Gamma/(a_\infty \lambda), \quad (2)$$

where λ is the wavelength of the incident acoustic waves, they computed scattered waves which have intense amplitude in the forward direction, and decay as $r^{-\frac{1}{2}}$ away from the outer radius. They also provided solutions in the limit of the inner radius going to zero, but there is some doubt about the validity of their limit process since the velocity field at the origin then tends to infinity (O'Shea 1975).

Finally, Candel (1979) solved for the scattered field numerically, using the parabolic approximation method, thus obtaining results valid near the forward scattering direction. In that case the scattering was found to be most intense in small bands located at about $\pm 15^\circ$ from the forward direction. His numerical computations were limited to a finite distance away from the vortex core, but over a distance of many times the core radius there was no apparent decay of the scattered field; he attributed this to refraction of the incident waves by the slowly decaying velocity field of the vortex.

A similar problem, that of acoustic destabilization of axisymmetric two-dimensional vortices by small azimuthal disturbances, was solved by Broadbent & Moore (1979).

Our own direct Navier–Stokes solutions of the scattering problem gives results similar to Candel's (1979). The amplitude of the scattered waves does not decay from outside the vortex core to the edge of the computational domain, and peak amplitude is found in bands centred about a small angle from the forward scattering direction.

To study the effect of scattering by the vortex core alone, computations are also performed for vortices for which $\Gamma = 0$. In that case the velocity field decays exponentially fast away from the vortex centre (Colonius, Lele & Moin 1991*b*), and therefore long-range refractive effects are not present. When the circulation is zero, the scattered acoustic waves decay as $r^{-\frac{1}{2}}$, and can be accurately predicted with a simple acoustic analogy. Tanaka & Ishii (1981) considered the scattering of plane sound waves by a vortex pair, for which the total circulation is zero, and also found a non-singular scattered field using the acoustic analogy of Yates (1978).

In §2 the numerical method for solving the Navier–Stokes equations is described, and results of the numerical experiments are presented. In §3 an approximate analytical solution is found, which attempts to account for the long-range refraction by retaining terms of order $\Gamma/(a_\infty \lambda)$ in the inviscid equations of motion. The solution is singular in the forward scattering direction, as in the analysis by O’Shea (1975), but the solution method gives the correct scattering away from the forward direction for all distances from the vortex core, and is correct in the forward direction up to at least moderate distances. In §4 a high-frequency approximation is solved to further examine the long-range refraction effects. In §5 the results are compared with experiment, and conclusions are placed in §6.

2. Direct numerical simulations with Navier–Stokes equations

2.1. Computational method

The two-dimensional compressible, unsteady Navier–Stokes equations are solved numerically on the computational domains shown in figure 2, which typically extend from 10 to 30 vortex core radii in each direction. To accurately resolve the propagation of the acoustic waves, finite difference and time marching schemes that have very low numerical dissipation and accurately represent the dispersion relation for the inviscid equations are required. To this end, sixth-order-accurate spatial derivatives are computed with a modified Padé-type scheme (Lele 1992), and solutions are advanced in time using a fourth-order-accurate Runge–Kutta scheme. When spatial derivatives near the computational boundary are needed, a third-order-accurate compact scheme biased towards the interior nodes is used. A uniform Cartesian mesh is used, with 7 to 8 grid points per vortex core radius in each direction.

Non-reflecting boundary conditions derived by Colonius *et al.* (1992) are used. These boundary conditions are based on a hierarchy of higher-order-accurate non-reflecting boundary conditions for the linearized Euler equations developed by Giles (1990). For the present problem, the zeroth-order boundary conditions are utilized. The interested reader is referred to Colonius *et al.* (1992) and Giles (1990) for a detailed derivation of these conditions. Both inflow and outflow boundary conditions are needed, since the vortex flow field alternates between positive and negative velocity normal to the computational boundary shown in figure 2. The boundary conditions rely on a decomposition of the flow near the computational boundaries into a steady base flow, and a unsteady perturbation field. The steady base flow at the boundaries is taken to be an inviscid compressible vortex whose tangential velocity is given by $\Gamma/(2\pi r)$. Outside the core the flow is essentially inviscid and steady until the time that the core has spread to the computational boundary. The computations are performed in the limit where the wavelength of the sound is larger than the core radius of the vortex, and therefore the time for viscous spreading of the vortex core is larger than the computational time required to compute the scattering of the incident waves, which effectively precludes interaction of the viscous core with the boundary.

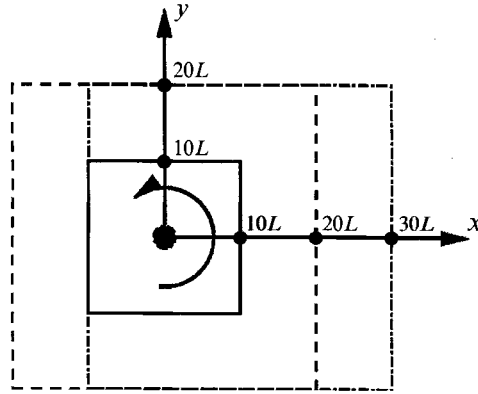


FIGURE 2. Computational Domains: —, Domain 1; ----, Domain 2; - · - ·, Domain 3.

The computations are initialized with a homentropic vortex. The tangential velocity is chosen to be

$$v_{\theta} = \frac{\Gamma}{2\pi r} (1 - \exp(-\alpha(r/L)^2)), \quad (3)$$

where $\alpha \approx 1.256431$ is a constant chosen such that the maximum velocity occurs at $r/L = 1$. If the radial velocity is set to zero, the preceding tangential velocity distribution is an exact solution of the incompressible viscous equations (Oseen vortex) where the core spreads in time such that $\alpha \sim 1/(\nu t)$, where ν is the kinematic viscosity. Equation (3) also satisfies the inviscid compressible equations if the radial velocity is zero. For both cases, the pressure satisfies

$$\partial p / \partial r = \rho v_{\theta}^2 / r, \quad (4)$$

where p and ρ are the pressure and density of the vortex, respectively. For an homentropic vortex, the density and pressure are related by

$$p / \rho^{\gamma} = \text{constant}, \quad (5)$$

where γ is the ratio of specific heats (taken to be 1.4 for air in what follows). For completeness, the pressure that satisfies (4) and (5) is given by:

$$p = \frac{\rho_{\infty} a_{\infty}^2}{\gamma} \left[1 - \frac{(\gamma - 1) \Gamma^2}{4 a_{\infty}^2 \pi^2 r^2} f(\alpha r^2 / L^2) \right]^{\frac{\gamma}{\gamma - 1}}, \quad (6)$$

where $f(x) = \frac{1}{2} - \exp(-x) + \frac{1}{2} \exp(-2x) + x \text{Ei}(-2x) - x \text{Ei}(-x), \quad (7)$

and where Ei is the exponential integral function (e.g. Abramowitz & Stegun 1972).

The exact solution for a vortex that is both compressible and viscous, and whose initial condition is given by (3), (5) and (6) was found by Colonius *et al.* (1991*b*). When the Reynolds number ($Re = v_{\theta_{max}} L / \nu$) of the vortex is large and the Mach number is small, this exact solution is different from the initial condition only to order M^2 / Re . We have used $Re = 10^5$ and Mach numbers ranging from 0.0625 to 0.5 in the computations, and therefore the numerical solution (without incoming sound waves) is well approximated by the initial condition for the duration of the computations.

Plane incident sound waves are generated at the left-hand computational boundary ($x = -10L$ for Domains 1 and 2 shown in figure 2, and $x = -20L$ for Domain 3). The peak amplitude of the particle velocity of the incident waves is 10^{-5} of the maximum vortex velocity, to ensure that the sound waves are well within the linear disturbance regime. The incident waves are allowed to travel through the entire computational domain. The scattered waves are directly measured from the computations as follows.

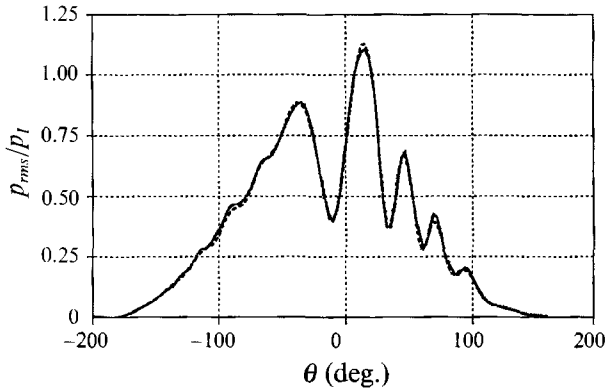


FIGURE 3. Comparison of root-mean-square pressure level of scattered wave, normalized by the amplitude of the incident waves, between simulations on different-sized domains: —, Domain 1; ---, Domain 2. See figure 2 for domain sizes.

Recall that the scattered wave field is defined as the difference between the fields that result from the interaction of the incident waves with the disturbance (vortex) flow field and the field that results with no incident disturbance. Thus, computationally, the scattered waves are obtained by subtracting the results of the computations with no incident sound waves from identical computations performed with incident sound and further subtracting the plane incident wave. Thus the slow viscous evolution of the vortex is effectively removed from the scattered field. The amplitude and phase of the scattered field computed by averaging over as many as four periods of the incident waves are identical to those computed over just one period, and thus the scattered field is monochromatic to a very high degree of accuracy. In other words the sound produced by initial transients and/or viscous effects is negligible. Also note that the Reynolds number relevant to the wave propagation, $Re_{wave} = \omega\lambda^2/\nu \approx 10^7$ (where ω is the frequency of the waves) and thus viscous attenuation of the waves is entirely negligible.

2.2. Validation of boundary conditions

A useful test of non-reflecting boundary conditions is a comparison of computations that are identical, except for the size of the computational domain. If the boundary conditions were perfectly non-reflecting, then the solution on the smaller domain would agree perfectly with the solution on the larger domain. The difference between the solutions gives an estimate of the error of the boundary conditions. The scattering from a vortex with finite circulation was computed on Domain 1 which extended to 10 core radii in each direction, and also on Domain 2, which extended to 30 core radii in the $+x$ -direction. The root-mean-square pressure amplitude of the scattered waves is plotted versus the angle from the forward ($+x$) direction, at $r = 10L$ in figure 3 for both computations. The r.m.s. pressure is normalized with the pressure amplitude (peak to peak) of the incident waves, p_I . The agreement between the two curves is good, the maximum difference between the scattering amplitudes for the smaller and larger domains being about 5%. For this particular flow, the zeroth-order boundary conditions, which are tantamount to assuming that the acoustic waves strike the boundary with normal incidence, appear to give sufficiently accurate results. We note that the zeroth-order boundary conditions are not adequate in more general flows, owing to both non-normal incidence of acoustic waves, and possible convection of large flow disturbances (such as a vortex) through the computational boundary (Colonius *et al.* 1992).



FIGURE 4. Iso-contours of the root-mean-square pressure level of the scattered wave, normalized by the amplitude of incident wave. Contour levels: Minimum = 0.08; Maximum = 1.12; Increment = 0.04. ($\epsilon = 0.27$, $\lambda/L = 4$, $M = 0.125$).

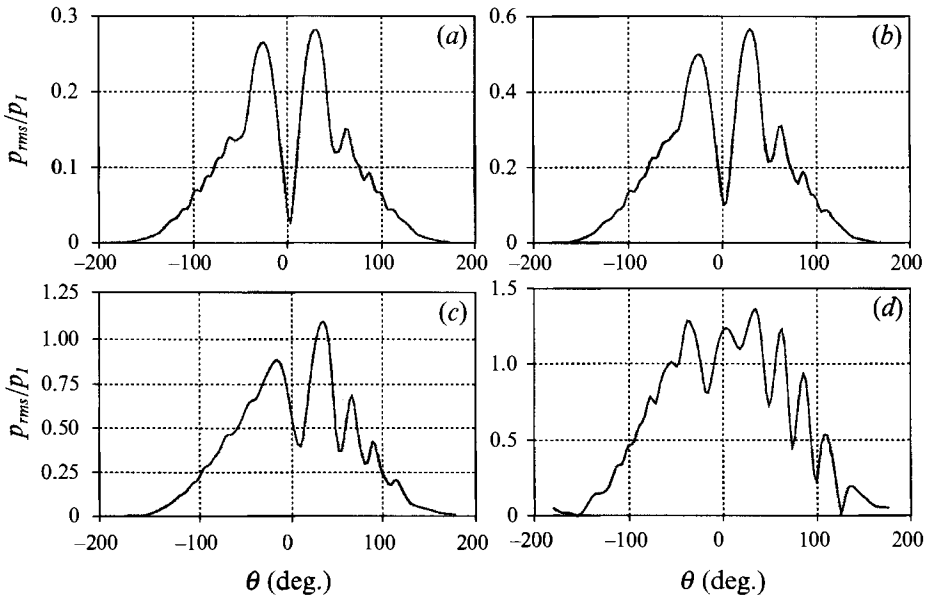


FIGURE 5. Root-mean-square pressure level of the scattered wave at $r = 2.5\lambda$. (a) $\epsilon = 0.14$ ($M = 0.0625$); (b) $\epsilon = 0.27$ ($M = 0.125$); (c) $\epsilon = 0.55$ ($M = 0.25$); (d) $\epsilon = 1.1$ ($M = 0.5$).

2.3. Simulation results

The scattered waves are directly computed as discussed above. Figure 4 shows contours of the root-mean-square pressure level of the scattered waves normalized by p_I for the conditions $\epsilon = 0.27$ and $\lambda/L = 4$ ($M = 0.125$). There is preferred scattering in the forward direction, and the scattering is asymmetrical with respect to the direction of incident propagation. The maximum scattering occurs at about 30° from the direction of incident propagation. Note that the contours shown in figure 4 are for a counterclockwise-spinning vortex; they should be reflected about $y = 0$ for a vortex that spins clockwise. Scattering in the backward direction is at least an order of magnitude smaller than in the forward direction.

In figure 5, the root-mean-square pressure scattering amplitude at $r = 2.5\lambda$ is plotted versus the angle with the direction of incident propagation, for $\lambda/L = 4$ and ϵ ranging

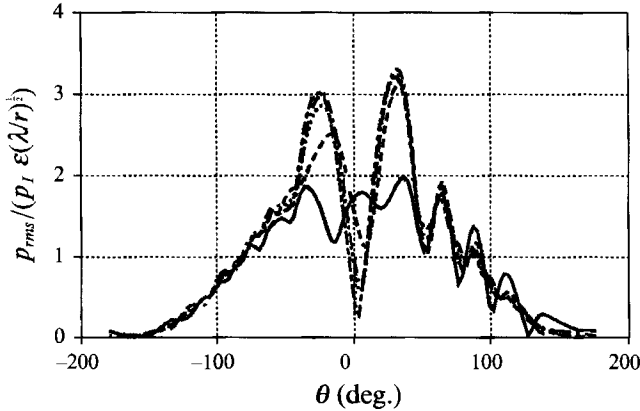


FIGURE 6. Root-mean-square pressure level at $r = 2.5\lambda$ normalized by the right-hand side of (8): —, $\epsilon = 1.1$, $\lambda/L = 4$ ($M = 0.5$); ---, $\epsilon = 0.55$, $\lambda/L = 4$ ($M = 0.25$); ·····, $\epsilon = 0.27$, $\lambda/L = 4$ ($M = 0.125$); — · —, $\epsilon = 0.14$, $\lambda/L = 4$ ($M = 0.0625$); - - - -, $\epsilon = 0.27$, $\lambda/L = 8$ ($M = 0.25$).

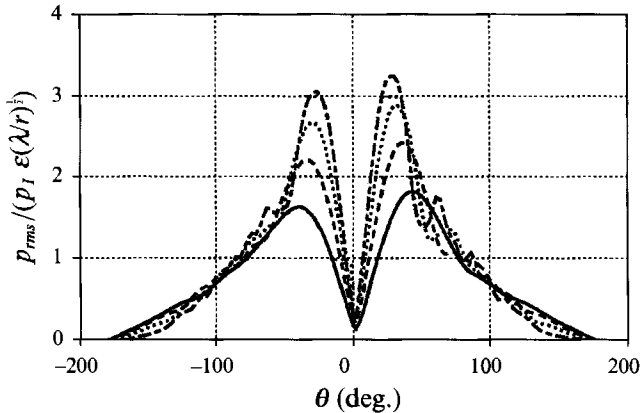


FIGURE 7. Root-mean-square pressure level normalized by right-hand side of (8); $\epsilon = 0.14$, $\lambda/L = 4$ ($M = 0.0625$): —, $r/\lambda = 1$; ---, $r/\lambda = 1.5$; ·····, $r/\lambda = 2$; — · —, $r/\lambda = 2.5$.

from 0.14 to 1.1 ($M = 0.0625$ to 0.5). A trend towards more asymmetrical distributions is clearly discernible as ϵ is increased, and in the top half-plane ($0^\circ < \theta < 180^\circ$) the amplitude becomes oscillatory. For the lowest value of ϵ , figure 5(a), the distribution is more nearly symmetric about $\theta = 0^\circ$, and as ϵ is reduced, the scattering at $\theta = 0^\circ$ appears to go to zero.

According to the low-frequency theories (e.g. O'Shea 1975) the root-mean-square pressure level should scale as

$$p_{rms} \sim p_i \epsilon (\lambda/r)^{\frac{1}{2}} \quad (8)$$

in the far-field, where p_i is the amplitude of the incident wave. In figure 6, the root-mean-square scattered pressure is normalized by the quantity on the right-hand side of (8), and plotted at $r/\lambda = 2.5$ for various values of ϵ and λ/L . As ϵ is reduced and λ/L is increased, the curves collapse and the scaling with ϵ appears to hold.

In figure 7, the scattered pressure level is plotted for different values of r/λ , with ϵ and λ/L fixed. Near the forward scattering direction ($\theta = 0^\circ$) the peak scattering does not scale like $(\lambda/r)^{\frac{1}{2}}$. The same curves are plotted in figure 8, but the pressure is not

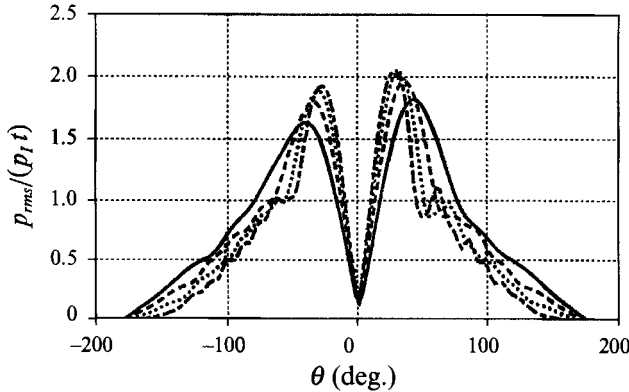


FIGURE 8. Root-mean-square pressure level normalized by $p_1 \epsilon$; $\epsilon = 0.14$, $\lambda/L = 4$ ($M = 0.0625$):
 —, $r/\lambda = 1$; ---, $r/\lambda = 1.5$; ·····, $r/\lambda = 2$; — · —, $r/\lambda = 2.5$.

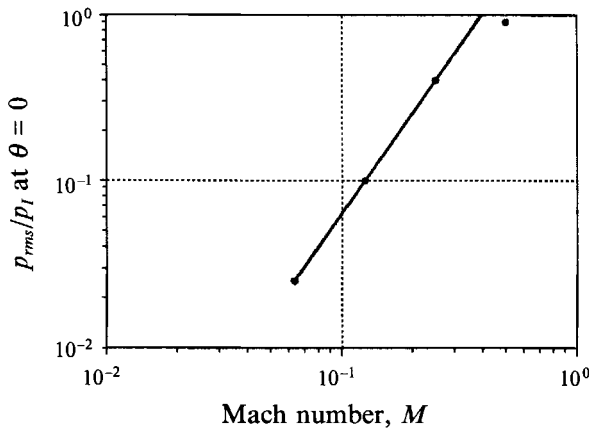


FIGURE 9. Scattering in the forward direction versus Mach number: ●, data from computations;
 —, line with slope 2.

normalized by the factor $(\lambda/r)^{\frac{1}{2}}$. In fact, figure 8 shows that the peak scattering is more nearly constant in r/λ . This lack of scaling with λ/r is attributed to refractive effects by the mean flow field, as will be discussed in the next section.

The compressible vortex has additional scattering effects due to the local change in the speed of sound, produced by the density inhomogeneity associated with the core. The scattering due to this effect should be symmetric about the direction of incident propagation, and when the Mach number is small (i.e. when ϵ is small) (5) and (6) imply that the density changes for the homentropic vortex are zero to $O(M^2)$. The finite scattering at $\theta = 0$ apparent in figure 5(a-d) is evidently the result of this effect, since the amplitude of the scattering at $\theta = 0$ scales very well with M^2 , as indicated by figure 9.

2.4. Comparison with aeroacoustic theory

Although the amplitude of the scattered wave is found to scale with the amplitude of the incident wave and the factor ϵ in accord with the aeroacoustic theories, the directivity pattern and far-field decay of the scattered field do not agree with any of the low-frequency predictions. The scattering amplitude goes to zero in the forward and reverse directions (in the limit as ϵ goes to zero), but the peak scattering angles are

much closer to the forward direction ($\pm 30^\circ$) than the dipole pattern predicted by Howe (1975), where the maximum would occur at ($\pm 90^\circ$). According to Yates (1978) the proper directivity is quadrupole, which is also not observed in the computations. The scattering is peaked about the forward direction, but in contrast to the far-field result of O'Shea (1975) it fails to obey the far-field scaling away from the vortex core. The stimulation results are qualitatively similar to the computations of Candel (1979) which indicate peak scattering to be at about $\pm 15^\circ$ from the forward direction. Moreover, the interference pattern and asymmetries evident in figure 5(a-d) are also present in his computations.

When refraction effects are neglected in the theories, the incident waves generated as $x \rightarrow -\infty$ in the analysis remain planar until interacting with the core. Since in the computations the waves are assumed to be planar at $x = -2.5\lambda$, and λ/L is always larger than 1, we conclude that generating the waves at a finite distance from the core cannot be responsible for the discrepancy with the results of previous theories. We also ruled out the role of different velocity distributions in the vortex core as the source of the discrepancy by performing a computation with a vorticity distribution similar to the 'top hat' distribution used in Howe (1975). Since a discontinuity in the vorticity is not permissible in the computations, we simulate the top-hat distribution with a vorticity that decays as $\exp(-r^n)$. For large n , this distribution approaches the top-hat distribution, while for $n = 2$ it gives the distribution corresponding to the velocity distribution used in the current computations. The scattering was also computed for $n = 6$, and it was found that the root-mean-square scattered pressure levels for $n = 6$ and $n = 2$ agreed to within less than 1%. Apparently core effects cannot explain the discrepancy between the analysis of Howe and the computations.

Candel (1979) attributes the disagreement between his computations and the aeroacoustic theories to the long-range refraction effect of the slowly decaying mean flow field. Theories that include the long-range refractive effects of the mean flow predict singular results in the forward direction. This is interpreted by O'Shea (1975) to mean that the Born approximation is not valid in the forward scattering direction. To further investigate refraction effects, a computation was conducted on a larger domain which extended to 20 vortex core radii in each direction, including the back scattering direction (labelled as Domain 3 in figure 2). Thus the incident sound waves generated at the boundary refract over distances twice as long as in the previous computations, before impinging on the vortex core. The scattering amplitude is plotted versus the observation angle at $r = 2.5\lambda$ in figure 10 for both the larger and smaller domains. The scattering amplitude is everywhere substantially greater for the larger domain, especially in the back scattering direction. In §3 we develop analytical solutions that account for the refraction effect.

2.5. Scattering from vortices with zero circulation

Since the apparent cause of the discrepancy between the computations and theories is the long-range refractive effect of the r^{-1} vortex flow field, it is of interest to compute the scattering from a compact vortex flow field. In two dimensions, when the circulation of the vortex is zero, the tangential velocity field decays exponentially fast for axisymmetric flow. We thus consider the scattering of sound waves by the swirling flow given by

$$u_\theta = u_{\theta_{max}} r \exp\left[\frac{1}{2}(1-r^2)\right], \quad (9a)$$

$$u_r = 0, \quad (9b)$$

$$p = (\rho_\infty a_\infty^2 / \gamma) (1 - \frac{1}{2}[(\gamma - 1) M^2 \exp(1 - (r/L)^2)])^{\frac{\gamma}{\gamma-1}}, \quad (9c)$$

$$\rho = \rho_\infty (\gamma p / (\rho_\infty a_\infty^2))^{\frac{1}{\gamma-1}}. \quad (9d)$$

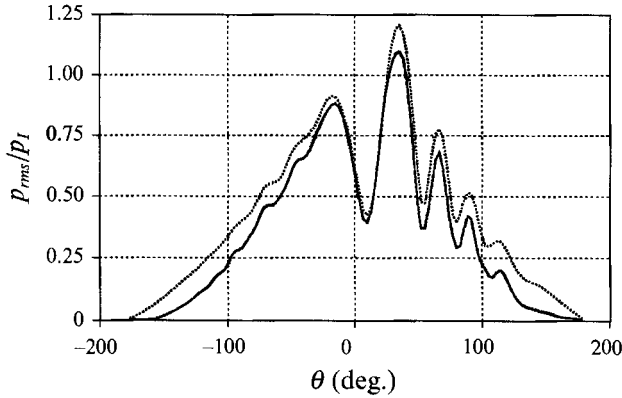


FIGURE 10. Comparison of root-mean-square pressure level of scattered wave between simulations on different sized domains. $\epsilon = 0.55$, $\lambda/L = 4$ ($M = 0.25$): —, Domain 1; ·····, Domain 3. See figure 2 for domain sizes.

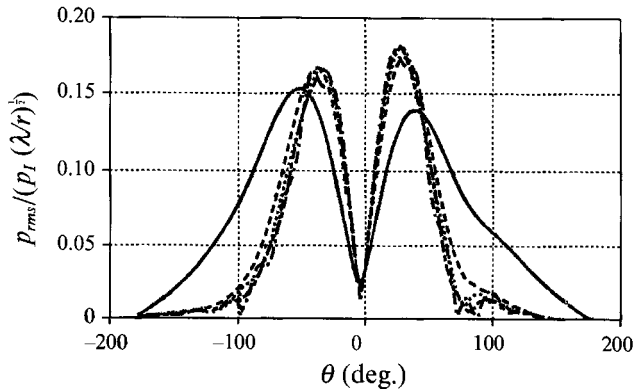


FIGURE 11. Root-mean-square pressure level of scattered waves, normalized by amplitude of incident wave and $(\lambda/r)^{1/2}$. $M = 0.125$, $\lambda/L = 4$: —, $r/\lambda = 0.5$; ---, $r/\lambda = 1.0$; ·····, $r/\lambda = 1.5$; -·-·-, $r/\lambda = 2.0$; — · —, $r/\lambda = 2.5$.

This inviscid solution is due originally to Taylor (1918). Except for the initial conditions, computations are performed in an identical manner as described for the finite-circulation vortex.

The root-mean-square density of the scattered waves is plotted as a function of the observation angle for increasing values of r/λ in figure 11. The density has been normalized by the amplitude of the incident waves, and the factor $(\lambda/r)^{1/2}$. The collapse of the curves for the larger values of λ/r plotted indicates that the far-field asymptotic behaviour has been reached by about $r/\lambda > 1$. This is in contrast to the finite-circulation scattering, which did not decay for $r/\lambda > 1$. The directivity pattern is similar to that of the finite-circulation vortex, with peak scattering occurring at about $\pm 30^\circ$ from the forward direction. The directivity pattern is significantly smoother than for the finite-circulation case, due apparently to the lack of refraction outside the vortex core. Again, a slight asymmetry about $\theta = 0$ is evident.

2.6. Comparison of zero-circulation scattering with acoustic analogy

Since the scattering amplitude decays like $r^{-1/2}$ away from the vortex core, we expect the acoustic analogy approach to accurately predict the scattering amplitude for the zero-circulation vortex. In this subsection we develop such an analogy. In §3 we modify the

analysis to account for the long-range refractive effects that dominate the scattering amplitude for the finite-circulation vortex.

Ignoring viscous effects, we start with the Euler equations for a perfect gas in cylindrical coordinates. The equations are linearized about a homentropic axisymmetric vortex with no radial velocity. The flow quantities are given by

$$u_r = u_r^d/a_\infty = u'_r(\tilde{r}, \theta, \tilde{t}), \quad (10a)$$

$$u_\theta = u_\theta^d/a_\infty = \bar{V}(\tilde{r}) + u'_\theta(\tilde{r}, \theta, \tilde{t}), \quad (10b)$$

$$\rho = \rho/\rho_\infty = \bar{\rho}(\tilde{r}) + \rho'(\tilde{r}, \theta, \tilde{t}), \quad (10c)$$

$$p = p^d/(\rho_\infty a_\infty^2) = \bar{p}(\tilde{r}) + p'(\tilde{r}, \theta, \tilde{t}), \quad (10d)$$

$$s = (s^d - s_\infty^d)/c_p = s'(\tilde{r}, \theta, \tilde{t}), \quad (10e)$$

where s is the entropy, c_v and c_p are the constant specific heats at constant volume and pressure respectively and the superscript d is used to denote dimensional quantities. Length and time have been normalized with respect to the frequency and wavelength of the incident sound:

$$\tilde{t} = 2\pi t^d a_\infty / \lambda, \quad \tilde{r} = 2\pi r^d / \lambda. \quad (11a, b)$$

The linearized equations are

$$\frac{\partial u'_r}{\partial \tilde{t}} + \frac{\bar{V}}{\tilde{r}} \frac{\partial u'_r}{\partial \theta} - 2 \frac{\bar{V}}{\tilde{r}} u'_\theta + \frac{1}{\bar{\rho}} \frac{\partial p'}{\partial \tilde{r}} - \frac{\bar{V}^2}{\tilde{r}} \frac{\rho'}{\bar{\rho}} = 0, \quad (12a)$$

$$\frac{\partial u'_\theta}{\partial \tilde{t}} + \frac{\bar{V}}{\tilde{r}} \frac{\partial u'_\theta}{\partial \theta} + \left(\frac{\partial \bar{V}}{\partial \tilde{r}} + \frac{\bar{V}}{\tilde{r}} \right) u'_r + \frac{1}{\bar{\rho} \tilde{r}} \frac{\partial p'}{\partial \theta} = 0, \quad (12b)$$

$$\frac{\partial \rho'}{\partial \tilde{t}} + \frac{\bar{V}}{\tilde{r}} \frac{\partial \rho'}{\partial \theta} + \frac{1}{\tilde{r}} \frac{\partial (\tilde{r} \bar{\rho} u'_r)}{\partial \tilde{r}} + \frac{\bar{\rho}}{\tilde{r}} \frac{\partial u'_\theta}{\partial \theta} = 0, \quad (12c)$$

$$\frac{\partial s'}{\partial \tilde{t}} + \frac{\bar{V}}{\tilde{r}} \frac{\partial s'}{\partial \theta} = 0, \quad (12d)$$

and

$$s' = (1/\bar{\rho})(p' - \bar{a}^2 \rho'), \quad (12e)$$

where $\bar{a}^2(\tilde{r})$ is the non-dimensional local speed of sound squared, $\bar{a}^2 = \gamma \bar{p}/\bar{\rho}$. Equations (12) can be rewritten as a wave equation for ρ' , by taking $\partial/\partial \tilde{t}$ of (12c) and subtracting $\partial/\partial \tilde{r} + 1/\tilde{r}$ of (12a) and $(1/\tilde{r})\partial/\partial \theta$ of (12b), and adding and subtracting the Laplacian of ρ' to both sides of the equation (as in Lighthill (1952)). The resulting equation is

$$\frac{\partial^2 \rho'}{\partial \tilde{t}^2} - \frac{1}{\tilde{r}} \frac{\partial}{\partial \tilde{r}} \left(\tilde{r} \frac{\partial \rho'}{\partial \tilde{r}} \right) - \frac{1}{\tilde{r}^2} \frac{\partial^2 \rho'}{\partial \theta^2} = S(\tilde{r}, \theta, \tilde{t}). \quad (13)$$

The particular form of S is algebraically complicated and not written here for brevity. It is of interest to note, however, that when the solution for the base vortex flow (equations (9)) are substituted into the source term S , and the result is expanded in powers of Mach number M , that the lowest-order terms in S are of order M , and that the entire term S thus decays exponentially fast for large \tilde{r} . When $M = 0$ (i.e. there is no vortex), (13) reduces to the homogeneous wave equation, which is satisfied by the plane incident sound waves. Thus if we set

$$\rho' = \rho'_{sc} + \rho'_I, \quad (14)$$

where the subscript I refers to the incident wave, and sc refers to the scattered wave, and note that incident wave satisfies (13) with $S = 0$, it follows that (13) applies if ρ' is substituted with ρ'_{sc} on the left-hand side.

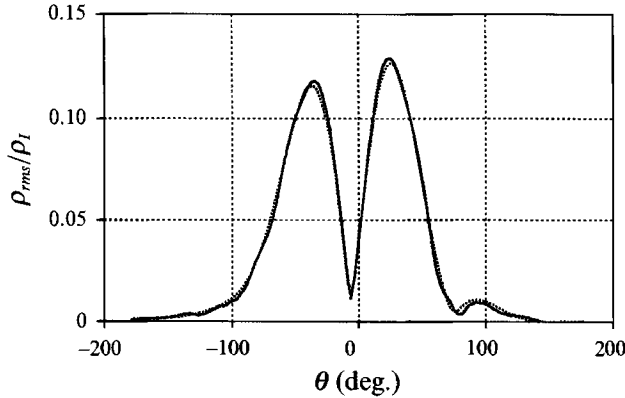


FIGURE 12. Comparison of root-mean-square density of scattered wave. —, Direct simulation results; ·····, computed from (18) with \hat{S} measured from computations. ($M = 0.125$).

If S is evaluated using the computed flow field, then the wave equation (13) can be inverted to give a prediction for the scattered waves. Since the computation results are monochromatic with the frequency of the incident waves, it is natural to set

$$\rho'_{sc} = \text{Re}(\hat{\rho}_{sc} \exp(-i\tilde{t})), \quad S = \text{Re}(\hat{S} \exp(-i\tilde{t})), \quad (15a, b)$$

from which it follows that

$$(\nabla^2 + 1)\hat{\rho}_{sc} = -\hat{S}. \quad (16)$$

The solution to (16) which obeys the Sommerfeld radiation condition at infinity (i.e. that there are no incoming waves aside from the incident sound waves already accounted for by (14)) is well known (e.g. Crighton 1975):

$$\hat{\rho}_{sc}(\mathbf{x}) = \int_{-\infty}^{\infty} \int_{-\infty}^{\infty} \frac{i}{4} \hat{S}(\mathbf{x}') H_0^{(1)}(|\mathbf{x} - \mathbf{x}'|) d\mathbf{x}'_1 d\mathbf{x}'_2. \quad (17)$$

The source term \hat{S} is evaluated from the results of the computations, and the integral in (17) is performed numerically, over the computational domain. The resulting root-mean-square density of the scattered waves is given by

$$\rho_{rms} = (1/2|\hat{\rho}_{sc}|^2)^{1/2} \quad (18)$$

and is plotted versus the observation angle in figure 12 for $r = 2\lambda$. Also plotted is the value of ρ_{rms} measured directly from the computations, which was given in figure 11. The curves agree to within a few percent. The excellent agreement between the directly computed and aeroacoustic analogy results indicate that the difficulties in direct computations of aeroacoustic fields mentioned in the introduction may be overcome. Evidently numerical discretization is not acting as a source of sound in the present computations, and the numerical accuracy is high enough to represent a wave field whose amplitude is five orders of magnitude smaller than the hydrodynamic field.

The source term \hat{S} can also be evaluated in the Born approximation. In that case, \hat{S} is expanded in powers of M , retaining only terms of $O(M)$. \hat{S} then takes on the simpler form

$$\hat{S} = -2\rho_1 M \sin \theta \tilde{r}\tilde{r}_0 (1 + i\tilde{r}\tilde{r}_0^2 \cos \theta) e^{i\tilde{r} \cos \theta} e^{(1-\tilde{r}^2\tilde{r}_0^2)/2}, \quad (19)$$

where $\tilde{r}_0 = 2\pi L/\lambda$. The presence of a dipole and quadrupole-type sources is indicated by the $\sin \theta$ and $\sin \theta \cos \theta$ terms respectively in (19).

The scattered wave amplitude evaluated in the Born approximation with source term (19) is compared in figure 13 to that computed with the source term measured from the

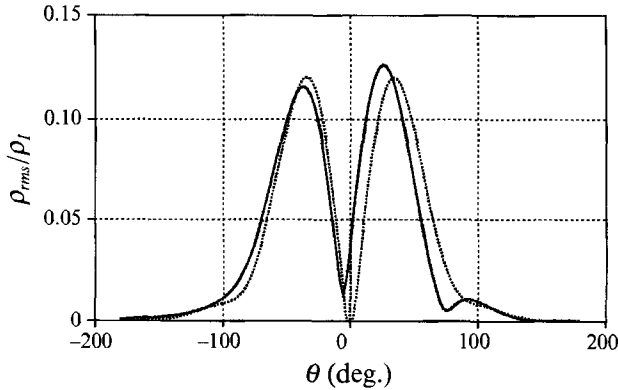


FIGURE 13. Comparison of root-mean-square density of scattered wave. —, Computed from (16) with \hat{S} measured from computations; ·····, computed with analytical source term given by (19). ($M = 0.125$).

computations. The difference between the two curves represents effects that are of higher order in M . The directivity pattern in the first scattering approximation is symmetrical, and is exactly zero in the forward direction. Hence the asymmetry in the directivity pattern, as well as the finite scattering in the forward direction are attributed to higher-order effects.

3. Analytical solution for finite-circulation vortices with small values of ϵ

When the circulation of the vortex is non-zero, the computations indicate that the scattering amplitude does not decay like $r^{-\frac{1}{2}}$ far from the vortex core. Long-range refraction by the slowly (r^{-1}) decaying mean flow field is apparently important. We now analyse the scattering of plane sound waves by a vortex with non-zero circulation. As in Müller & Matschat (1959), we express the Born, or low-frequency, approximation by demanding

$$\epsilon = \Gamma / (a_\infty \lambda) \ll 1. \tag{20}$$

We then expand the Euler equations linearized about the vortex flow field in a power series in ϵ for small values of ϵ .

To simplify the analysis, the tangential velocity of the vortex flow field is represented by a core in solid-body rotation surrounded by the flow field of an irrotational point vortex. The tangential velocity is

$$\bar{V}(\tilde{r}) = \begin{cases} \epsilon \tilde{r} / \tilde{r}_0^2, & \tilde{r} < \tilde{r}_0; \\ \epsilon / \tilde{r}, & \tilde{r} > \tilde{r}_0, \end{cases} \tag{21}$$

where $\tilde{r}_0 = 2\pi L / \lambda$, and L is the core radius of the vortex, as previously defined. As shown in the last section, the scattering of waves by (21) is not likely to be significantly different from the more realistic profile (3).

Solving (4) gives for the base pressure

$$\bar{p}(\tilde{r}) = \begin{cases} \frac{1}{\gamma} \left[1 - \frac{1}{2}(\gamma - 1) \epsilon^2 \left(2 - \left(\frac{\tilde{r}}{\tilde{r}_0} \right)^2 \right) \right]^{\frac{\gamma}{\gamma-1}}, & \tilde{r} < \tilde{r}_0; \\ \frac{1}{\gamma} \left[1 - \frac{(\gamma - 1) \epsilon^2}{2(\tilde{r} / \tilde{r}_0)^2} \right]^{\frac{\gamma}{\gamma-1}}, & \tilde{r} > \tilde{r}_0. \end{cases} \tag{22}$$

We now suppose that $\epsilon \ll 1$. Expanding f in a Taylor series about $\epsilon = 0$, where f is any of ρ' , p' , u'_r , u'_θ , or s' we write

$$f = f_0 + \epsilon f_1 + \epsilon^2 f_2 + \dots \quad (23)$$

It is assumed that there are no incoming entropy disturbances, so that $s' = 0$; then (12e) implies

$$p'_0 = \rho'_0 \quad \text{and} \quad p'_1 = \rho'_1, \quad (24a, b)$$

and expanding (12) using (23) gives, to zeroth order in ϵ ,

$$\frac{\partial^2 \rho'_0}{\partial \tilde{t}^2} - \frac{1}{\tilde{r}} \frac{\partial}{\partial \tilde{r}} \left(\tilde{r} \frac{\partial \rho'_0}{\partial \tilde{r}} \right) - \frac{1}{\tilde{r}^2} \frac{\partial^2 \rho'_0}{\partial \theta^2} \equiv \frac{\partial^2 \rho'_0}{\partial \tilde{t}^2} - \nabla^2 \rho'_0 = 0. \quad (25)$$

Note that the requirement $\epsilon \ll 1$ also places a restriction on the wavelength of the incident sound compared to the vortex core radius since it implies that

$$\epsilon \ll 1 \Leftrightarrow \tilde{r}_0 \ll 1/M. \quad (26)$$

Plane incident waves identically satisfy (25), and so we take the solution to zeroth order to be

$$\rho'_0 = \rho_I \exp i(\tilde{x} - \tilde{t}) = \rho_I \exp i(\tilde{r} \cos \theta - \tilde{t}), \quad (27)$$

The particle velocities of the incident waves in the (\tilde{r}, θ) coordinate system are

$$u'_{r0} = \rho_I \cos \theta \exp i(\tilde{r} \cos \theta - \tilde{t}), \quad (28a)$$

$$u'_{\theta 0} = -\rho_I \sin \theta \exp i(\tilde{r} \cos \theta - \tilde{t}). \quad (28b)$$

Retaining terms of order ϵ in (12) gives

$$\epsilon \left(\frac{\partial u'_{r1}}{\partial \tilde{t}} + \frac{\partial \rho'_1}{\partial \tilde{r}} \right) = -\frac{\bar{V}}{\tilde{r}} \frac{\partial u'_{r0}}{\partial \theta} + 2 \frac{\bar{V}}{\tilde{r}} u'_{\theta 0}, \quad (29a)$$

$$\epsilon \left(\frac{\partial u'_{\theta 1}}{\partial \tilde{t}} + \frac{1}{\tilde{r}} \frac{\partial \rho'_1}{\partial \theta} \right) = -\frac{\bar{V}}{\tilde{r}} \frac{\partial u'_{\theta 0}}{\partial \theta} - \left(\frac{\partial \bar{V}}{\partial \tilde{r}} + \frac{\bar{V}}{\tilde{r}} \right) u'_{r0}, \quad (29b)$$

$$\epsilon \left(\frac{\partial \rho'_1}{\partial \tilde{t}} + \frac{1}{\tilde{r}} \frac{\partial (\tilde{r} u'_{r1})}{\partial \tilde{r}} + \frac{1}{\tilde{r}} \frac{\partial u'_{\theta 1}}{\partial \theta} \right) = -\frac{\bar{V}}{\tilde{r}} \frac{\partial \rho'_0}{\partial \theta}. \quad (29c)$$

We seek solutions of (29) that are monochromatic with the frequency of the incident waves, $2\pi a_\infty/\lambda$. Thus let

$$\rho'_1(\tilde{r}, \theta)/\rho_I = \text{Re}(\hat{\phi} \exp(-i\tilde{t})). \quad (30)$$

As before, (29) can be transformed to

$$\hat{\phi} + \frac{1}{\tilde{r}} \frac{\partial}{\partial \tilde{r}} \left(\tilde{r} \frac{\partial \hat{\phi}}{\partial \tilde{r}} \right) + \frac{1}{\tilde{r}^2} \frac{\partial^2 \hat{\phi}}{\partial \theta^2} = -2A \sin \theta \exp(i\tilde{r} \cos \theta) S(\tilde{r}, \theta), \quad (31)$$

where (30) has been used and where

$$S(\tilde{r}, \theta) = \begin{cases} \tilde{r}/\tilde{r}_0^2, & \tilde{r} < \tilde{r}_0; \\ \frac{1}{\tilde{r}} + \frac{2i \cos \theta}{\tilde{r}^2}, & \tilde{r} > \tilde{r}_0. \end{cases} \quad (32)$$

Equation (31) is the Helmholtz equation written in cylindrical coordinates. Note the part of the source term (32) that decays as $1/\tilde{r}$ for large \tilde{r} is the result of the $1/\tilde{r}$ decay

of the base velocity field outside the vortex core. Convolution of the source term S with the free-space Green's function

$$G(\mathbf{x}) = \frac{1}{4i} H_0^{(1)}\left(\frac{2\pi|\mathbf{x}|}{\lambda}\right) \tag{33}$$

may produce a divergent integral, at least for some values of θ . If the solution for $\hat{\phi}$ diverges, then the scattered field is not well defined in the Born approximation. O'Shea (1975) evaluates a similar integral asymptotically and finds an infinite scattering amplitude in the forward direction, $\theta = 0$, but claims that the result is valid in directions far from the forward direction, where he obtains a quadrupole scattering amplitude which decays as $\tilde{r}^{-\frac{1}{2}}$, in contrast to our numerical experiments. Instead, we try to solve the integral *exactly*, but in a different form. Note that the coefficients on the left-hand side of (31) do not depend on θ , and therefore it is natural to expand (31) in terms of its Fourier coefficients in the azimuthal direction. The Fourier expansion is

$$\hat{\phi}^m(\tilde{r}) = \frac{1}{2\pi} \int_0^{2\pi} \hat{\phi}(\tilde{r}, \theta) \exp(-i\theta m) d\theta, \tag{34a}$$

$$\hat{\phi}(\tilde{r}, \theta) = \sum_{m=-\infty}^{\infty} \hat{\phi}^m \exp(i\theta m), \tag{34b}$$

which transforms (31) into an inhomogeneous second-order ordinary differential equation,

$$\frac{d^2 \hat{\phi}^m}{d\tilde{r}^2} + \frac{1}{\tilde{r}} \frac{d\hat{\phi}^m}{d\tilde{r}} + \left(1 - \frac{m^2}{\tilde{r}^2}\right) \hat{\phi}^m = \hat{S}^m(\tilde{r}), \tag{35}$$

where

$$\hat{S}^m(\tilde{r}) = \begin{cases} \frac{2mi^m J_m(\tilde{r})}{\tilde{r}_0^2}, & \tilde{r} < \tilde{r}_0; \\ 2mi^m \left(\frac{J_m(\tilde{r})}{\tilde{r}^2} + \frac{2J'_m(\tilde{r})}{\tilde{r}^3} - \frac{2J_m(\tilde{r})}{\tilde{r}^4}\right), & \tilde{r} > \tilde{r}_0, \end{cases} \tag{36}$$

in which J_m is the m th-order Bessel Function of the first kind and the prime denotes differentiation with respect to \tilde{r} .

Note that the source term for each Fourier mode, m , decays in \tilde{r} one power faster than does the source term in the physical space for $\tilde{r} > \tilde{r}_0$. Thus there is no problem in writing down the general solution to (35). However, we should keep in mind that the Fourier sum (34b) may not converge for certain values of θ , where the original integral diverges.

The general solution to (35) is

$$\begin{aligned} \hat{\phi}^m = C_{1m} J_m(\tilde{r}) + C_{2m} Y_m(\tilde{r}) - \frac{1}{2} J_m(\tilde{r}) \int^{\tilde{r}} \pi x Y_m(x) \hat{S}^m(x) dx \\ + \frac{1}{2} Y_m(\tilde{r}) \int^{\tilde{r}} \pi x J_m(x) \hat{S}^m(x) dx, \end{aligned} \tag{37}$$

where Y_m is the m th-order Bessel Function of the second kind. The arbitrary constants C_{1m} and C_{2m} (or alternatively the lower limits of integration) in (37) must be determined from suitable boundary conditions. At the origin, the solution is required

to be bounded. As $\tilde{r} \rightarrow \infty$, there should no incoming waves, except for the incident sound waves, which are already accounted for in the zeroth-order solution. Thus a radiation condition may be applied to each azimuthal mode. That is, as $\tilde{r} \rightarrow \infty$

$$\lim_{\tilde{r} \rightarrow \infty} \tilde{r}^{\frac{1}{2}} \left(\frac{d\hat{\phi}^m}{d\tilde{r}} - i\hat{\phi}^m \right) = 0. \quad (38)$$

Performing the integrations in (37), the general solution is

$$\hat{\phi}^m(\tilde{r}) = \begin{cases} C_{1m}^- J_m + C_{2m}^- Y_m - mi^m \left(\frac{\tilde{r}}{\tilde{r}_0} \right)^2 \frac{J'_m}{\tilde{r}}, & \tilde{r} < \tilde{r}_0; \\ C_{1m}^+ J_m + C_{2m}^+ Y_m - mi^m \frac{J_m}{\tilde{r}^2} \\ \quad + \pi i^m \left[Y_m \sum_{n=m}^{\infty} J_n^2 + J_m \left(\sum_{n=1}^{m-1} J_n Y_n + \frac{1}{2} J_0 Y_0 \right) \right], & \tilde{r} > \tilde{r}_0, \end{cases} \quad (39)$$

where the Bessel functions are to be evaluated at \tilde{r} .

For $\tilde{r} \rightarrow 0$ the solution must be bounded and thus

$$C_{2m}^- = 0. \quad (40)$$

Taking the limit in (37) gives a relation between the constants:

$$C_{2m}^+ = iC_{1m}^+ - \frac{1}{2}\pi im. \quad (41)$$

The remaining constants, C_{1m}^- and C_{1m}^+ are determined by forcing the solutions to match at $\tilde{r} = \tilde{r}_0$. This yields

$$C_{1m}^- = C_{1m}^+ = \frac{1}{2}\pi i^{(m-1)} - mi^m \frac{J'_m(\tilde{r}_0)}{\tilde{r}_0} + mi^m \frac{J_m(\tilde{r}_0)}{\tilde{r}_0^2} - \pi i^m \left[Y_m(\tilde{r}_0) \sum_{n=m}^{\infty} J_n^2(\tilde{r}_0) + J_m(\tilde{r}_0) \left(\sum_{n=1}^{m-1} J_n(\tilde{r}_0) Y_n(\tilde{r}_0) + \frac{1}{2} J_0(\tilde{r}_0) Y_0(\tilde{r}_0) \right) \right]. \quad (42)$$

The solution for each mode m is thus determined, and the scattered field can be found by summing the Fourier series. Noting that

$$\hat{\phi}^m = -\hat{\phi}^{-m}, \quad (43)$$

the root-mean-square scattered wave amplitude is given by

$$\rho_{rms} = \rho_I e^{-\frac{1}{\sqrt{2}}} \left| 2i \sum_{m=1}^{\infty} \hat{\phi}^m \sin(i\theta m) \right|. \quad (44)$$

The sum in (44) is performed numerically by summing over a finite number of modes, and is converged to computer roundoff. The resulting scattering amplitude is shown in figure 14(a) for the same radii and values of the parameters as in figure 8. A qualitative agreement between the analytical result (figure 14) and the computational result (figure 8) is observed. The scattering amplitude continues to grow outside vortex core region, the maximum scattering occurring at angles nearer the forward scattering direction as r is increased. This is contrasted with the $r^{-\frac{1}{2}}$ scaling of the zero-circulation vortex observed in the previous section. In figure 14(b) the analytical scattering amplitude is plotted for larger values of \tilde{r} , where the maximum scattering amplitude continues to grow.

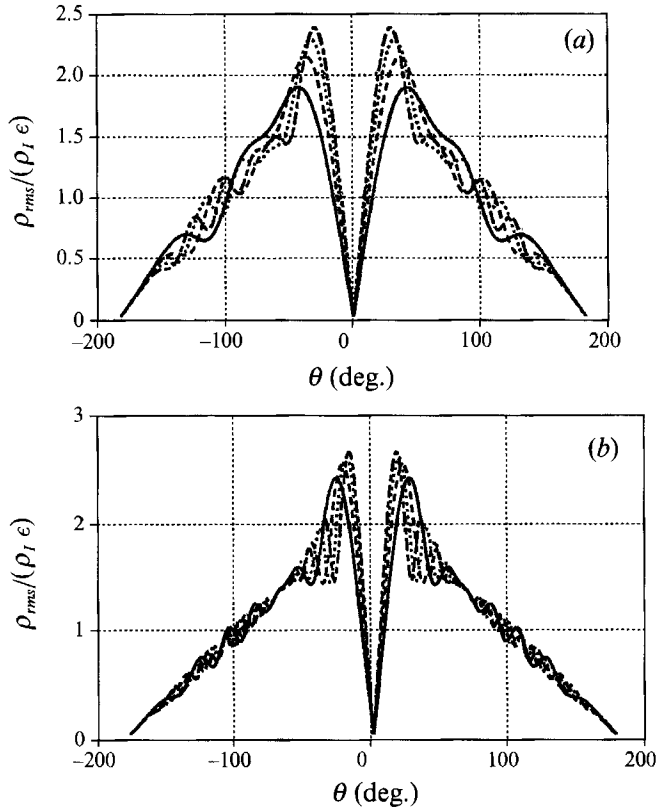


FIGURE 14. Root-mean-square density level from analysis, (44). (a) $\lambda/L = 4$: —, $r/\lambda = 1$; ----, $r/\lambda = 1.5$; ·····, $r/\lambda = 2$; —·—, $r/\lambda = 2.5$. (b) $\lambda/L = 4$: —, $r/\lambda = 3$; ----, $r/\lambda = 4.5$; ·····, $r/\lambda = 6.0$; —·—, $r/\lambda = 7.5$.

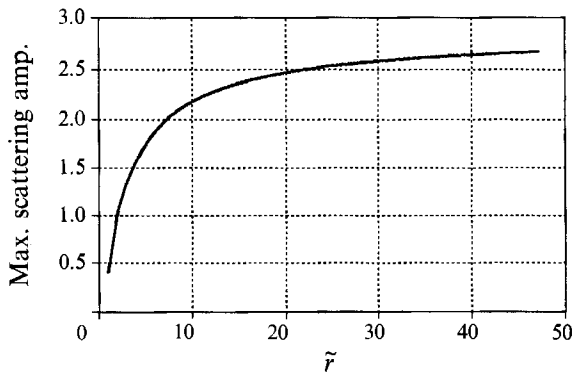


FIGURE 15. Maximum scattering amplitude versus \tilde{r} ; $\tilde{r}_0 = \frac{1}{2}\pi$.

The scattering amplitude away from $\theta = 0$ apparently becomes constant as \tilde{r} is increased, with an increasing number of oscillations of progressively smaller amplitude.

The maximum scattering amplitude is plotted versus \tilde{r} in figure 15. It is not possible to plot the values for larger values of \tilde{r} , owing to accumulation of roundoff errors in the summation of the series. We have tried to determine from the available data if the

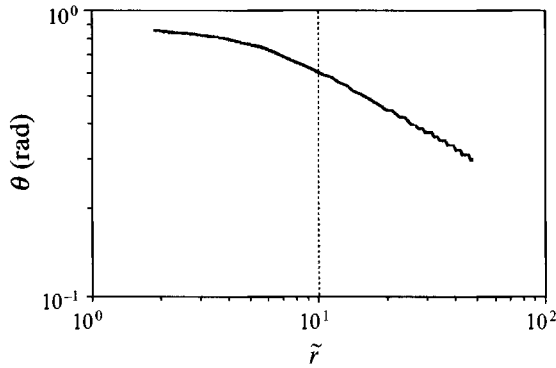


FIGURE 16. Angle where maximum scattering amplitude occurs versus \tilde{r} ; $\tilde{r}_0 = \frac{1}{2}\pi$.

curve asymptotes to a constant value or diverges, but it is impossible to draw a firm conclusion. If the curve diverges, it is apparently more slowly than logarithmically. At any rate, the result is undoubtedly singular for $\theta = 0$, since the angle where the maximum scattering occurs continues to decrease towards $\theta = 0$ as \tilde{r} is increased. In figure 16 the angle where the maximum occurs is plotted versus \tilde{r} in log-log coordinates, indicating that the angle decreases towards zero at a rate of $r^{-\frac{1}{2}}$.

Evidently a far-field scaling (a $r^{-\frac{1}{2}}$ decay of the amplitude) is never reached. This would seem to indicate the presence of a plane wave component of the scattered waves, as was found by O'Shea, far from the vortex core – evidently due to the long-range refraction by the slowly decaying vortex flow field.

We have not been able to determine exactly why there is a discrepancy between O'Shea's result away from the singular directions and the above result and the computations. However, note that if we replace the Bessel functions in (39) by their asymptotic expansions and (incorrectly) retain only the most slowly decaying powers of \tilde{r} , then the sum (44) can be written

$$\rho_{rms} = 2\rho_I \epsilon \left(\frac{1}{\pi\tilde{r}}\right)^{\frac{1}{2}} \left| \sum_{m=1}^{\infty} (-i)^m C_{1m}^+ \sin(m\theta) \right|. \tag{45}$$

For the case shown in figure 14, the values of $(-i)^m C_{1m}^+$ are equal to $-\frac{1}{2}i\pi$ for m greater than 3. Split the sum (45) into two parts:

$$\rho_{rms} = 2\rho_I \epsilon \left(\frac{1}{\pi\tilde{r}}\right)^{\frac{1}{2}} \left| \sum_{m=1}^{\infty} \left(-\frac{1}{2}i\pi\right) \sin(m\theta) + \sum_{m=1}^2 \left((-i)^m C_{1m}^+ - \frac{1}{2}i\pi\right) \sin(m\theta) \right|. \tag{46}$$

Now, the first sum in (46) can be found analytically:

$$\sum_{m=1}^{\infty} -i \sin(m\theta) = -\frac{1}{2}i \cot\left(\frac{1}{2}\theta\right). \tag{47}$$

This is exactly the singular term found by O'Shea. However, it is not the proper asymptotic expansion of (44). Since the constants C_{1m}^+ remain finite for large m , there are always terms in the series for which the asymptotic expansion of the Bessel functions for large argument will not hold.

Although the analytical result agrees fairly well with the computations, for small to moderate values of \tilde{r} , it is still singular (and possibly divergent) in the forward direction for large values of \tilde{r} . If it diverges, then the original expansion given by (23) cannot hold

in that region. This would indicate that the problem may not be physically well-posed,† and that one cannot require the incident and refracted waves to travel over very large distances through the \tilde{r}^{-1} velocity field without becoming significantly distorted. However, away from the forward direction, the amplitude becomes constant as \tilde{r} is increased, and therefore the analytical result should be valid for large \tilde{r} away from the forward direction. The agreement with the computational results would seem to indicate the result is also valid in the forward direction, at least for small to moderate values of \tilde{r} .

Finally, note that the lack of a strict quantitative agreement between the computational result (figure 8) and the analytical result (figure 14), especially in the backward scattering direction, is likely because the incident waves are generated at a finite distance from the vortex core in the computations, which is confirmed by the high-frequency analysis presented in the next section.

4. High-frequency solution for finite-circulation vortices

In order to confirm the scaling with \tilde{r} of the long-wavelength approximation, and to understand the lack of quantitative agreement between the long-wavelength approximation and the Navier–Stokes computations, we now analyse the refraction of plane incident waves by the finite-circulation vortex using the high-frequency approximation. When the frequency of the incident sound is large, the refraction of the waves through the flow field can be determined by the technique of ray tracing. In the notation of §3, we require that

$$2\pi L/\lambda = \tilde{r}_0 \gg 1. \quad (48)$$

The Navier–Stokes computations reported in §2 used $\tilde{r}_0 = \frac{1}{2}\pi$.

Georges (1972) computed the ray paths through a viscous vortex represented by (3) in the high-frequency limit, but did not determine the amplitude of the waves. We will extend the analysis to determine the amplitude and phase of the waves as they travel through the viscous vortex. The details of the analysis are in the Appendix, since standard methods are used. The waves are again considered to be monochromatic, and they are initiated as plane waves at some finite distance $-x_0$ from the vortex centre. The distance x_0 can be increased to very large values to compare with the analytical solutions of §3, or set equal to $10L$ to compare with the Navier–Stokes computations (it would be too expensive to extend the Navier–Stokes computations to large values of x_0). The problem configuration is the same as shown in figure 1.

The ray paths through the vortex are shown in figure 17, for the four values of ϵ shown in figure 5, for $x_0 = 10L$. The axes are normalized such that the core radius is 1. The ray paths are independent of \tilde{r}_0 , for $\tilde{r}_0 \gg 1$. The ray paths are in good agreement with those reported by Georges (see, for example, Georges' figure 2). A pair of caustics is formed by the rays which travel through the upper half of the vortex core, separating the diffraction into two regions. In between the two caustic lines there are three paths crossing any given point, while outside the lines there is only one. The location of the caustic is shown in figure 18, for the $\epsilon = 0.55$ case. The area between the caustics decreases as ϵ is decreased, the region approaching (at large distances) a small wedge around $\theta = 0$.

The amplitude of the waves long the rays was also computed, by carrying the analysis to the second order. Again the details can be found in the Appendix. Near the caustics, the linear ray theory breaks down since adjacent rays converge, giving an

† We would like to thank one of the Referees for pointing this out.

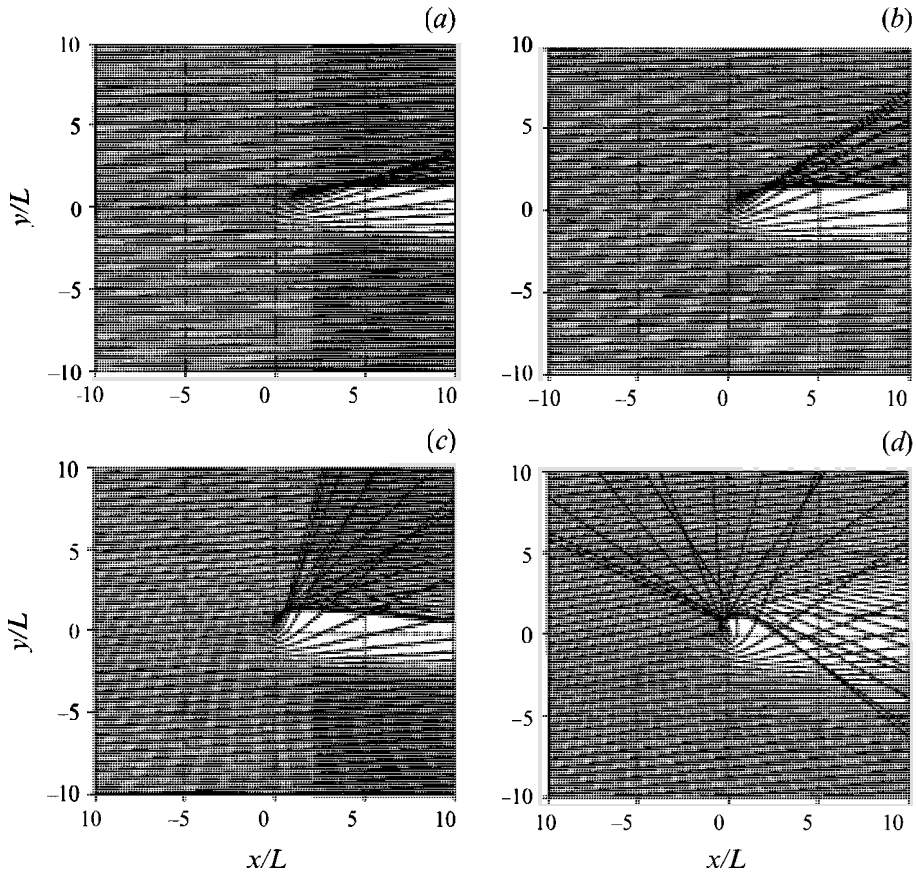


FIGURE 17. Ray paths through finite-circulation vortex. (a) $\epsilon = 0.14$, (b) $\epsilon = 0.27$, (c) $\epsilon = 0.55$, (d) $\epsilon = 1.1$.

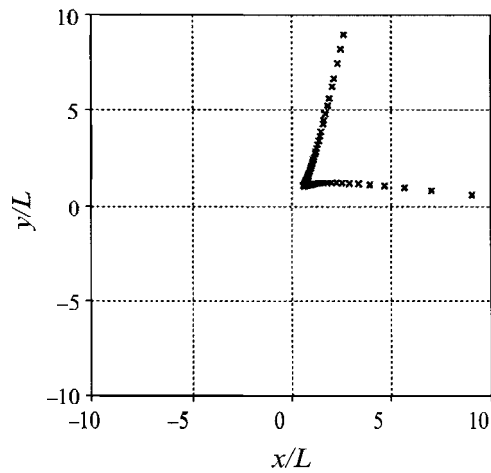


FIGURE 18. Location of caustic for $\epsilon = 0.55$.

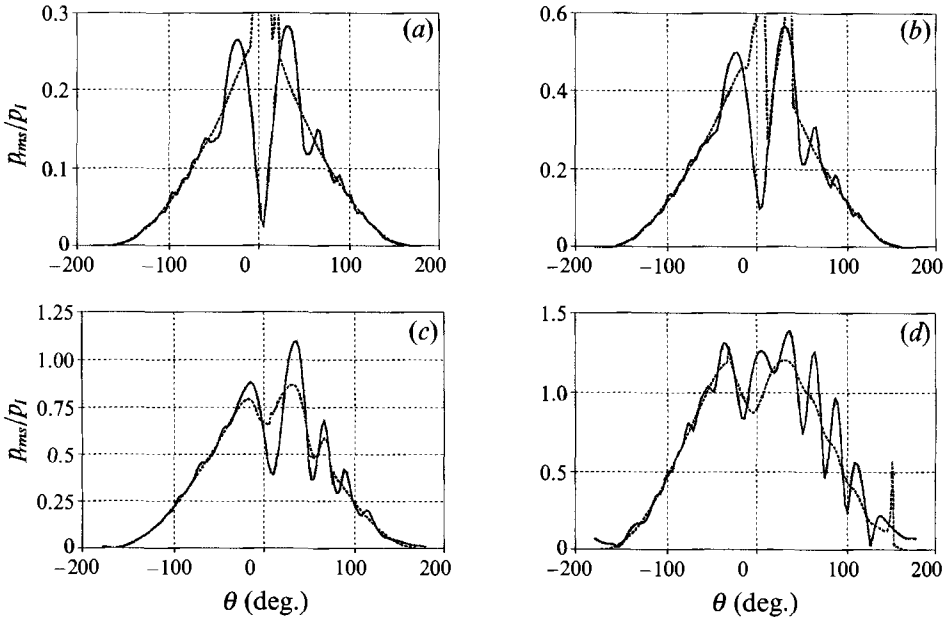


FIGURE 19. Root-mean-square pressure level of scattered wave at $r = 2.5\lambda$. (a) $\epsilon = 0.14$, (b) $\epsilon = 0.27$, (c) $\epsilon = 0.55$, (d) $\epsilon = 1.1$. —, Navier–Stokes solutions with $\tilde{r}_0 = \frac{1}{2}\pi$; ----, high-frequency approximation.

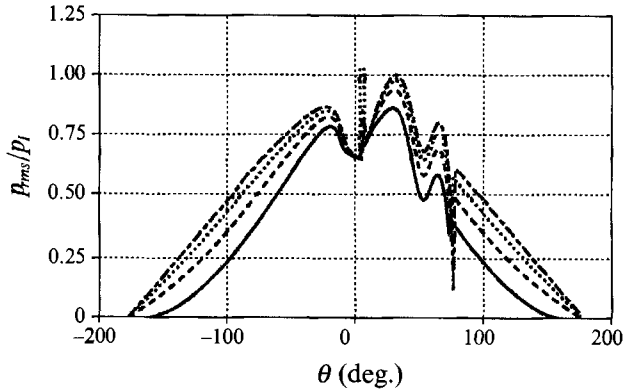


FIGURE 20. High-frequency scattering amplitude for $\epsilon = 0.55$. —, $x_0 = 10$; ----, $x_0 = 20$; , $x_0 = 40$; — · —, $x_0 = 100$.

infinite amplitude. The correct amplitude near the caustics must be determined by patching the solution with the Airy function across the caustic, which we have not attempted. The amplitude of the waves is plotted in figure 19 for the four values of ϵ plotted in figures 5 and 17, for $\tilde{r} = 5\pi$ ($r/\lambda = 2.5$). The amplitude of the plane wave has been subtracted to facilitate comparison with the scattering computations of §2, which are replotted in figure 19. The large spikes in the curves indicate the angle where the caustics cross the measurement arc, where the solution is invalid. Away from the caustics, the agreement is good, especially in the backward scattering direction. In the forward direction the high-frequency solution does not exhibit the interference pattern to the same degree as seen in the Navier–Stokes solution. This is likely due to the

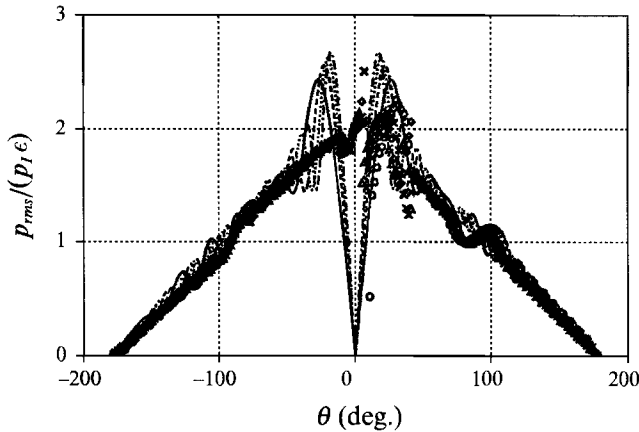


FIGURE 21. High-frequency scattering amplitude compared with long-wavelength analytical solution. Lines are from long-wavelength analysis, $\tilde{r}_0 = \frac{1}{2}\pi$: —, $r/\lambda = 3$; ----, $r/\lambda = 4.5$; ·····, $r/\lambda = 6.0$; — — —, $r/\lambda = 7.5$. Symbols are from high-frequency approximation with $\epsilon = 0.30$: \circ , $r/\lambda = 3$; \times , $r/\lambda = 4.5$; \diamond , $r/\lambda = 6.0$; \triangle , $r/\lambda = 7.5$. $x_0 = 200$.

relatively small value of $\tilde{r}_0 = \frac{1}{2}\pi$, given that the high-frequency solution is most accurate for $\tilde{r}_0 \gg 1$.

Figure 20 shows the wave amplitude for $\epsilon = 0.55$ as x_0 , the distance from the vortex centre where the plane waves are initiated, is increased. As the waves are initiated at larger distances from the vortex, the scattering increases everywhere and the curves look more and more like the analytical solution for small ϵ given in §3. For $x_0 = 100$, the amplitude away from forward direction varies more or less linearly with θ , as does the analytical solution for small ϵ (see figure 14).

The high-frequency solution is compared directly with the long-wavelength analytical solution in figure 21: \tilde{r}_0 is again taken as $\frac{1}{2}\pi$, but the waves are started even farther from the vortex core, with $x_0 = 200$. The scattering at four different values of \tilde{r} is plotted in figure 21, the agreement being good for each, except near the forward direction where the caustics cause the high-frequency solution to be invalid. The conclusion from the plot is that the high-frequency solution gives the same scaling with \tilde{r} as does the analytical solution, lending further evidence that the analytical solution is correct, at least for small to moderate values of \tilde{r} . It also confirms that the lack of quantitative agreement between the Navier–Stokes computations and the analytical solution is due to the difference in the location where the plane incident waves are generated.

5. Comparison with experiments

The scattered field arising from the incidence of monochromatic plane sound waves on a steady vortex has been measured experimentally by Horne (1983). In the experiment, a vortex is formed between two parallel disks 30.5 cm in diameter spaced 5.1 cm apart. The vortex is created by three tangential air jets located on each disk at a radius of 10.2 cm. The vortex is made steady by removing $0.0047 \text{ m}^3 \text{ s}^{-1}$ of air from the vortex core through suction ports at the centre of each disk. Plane sound waves were generated with a rectangular horn radiator with an opening of 15.2 cm by 5.1 cm, which is located at a radius just beyond the tangential air jets and the acoustic field was measured with a 1.27 cm condenser microphone traversed along a circular arc of

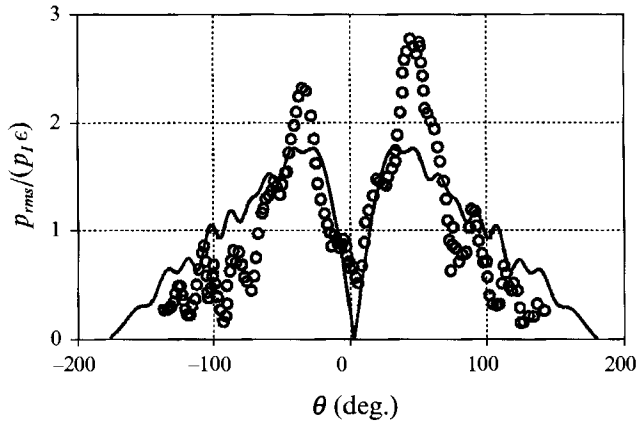


FIGURE 22. Comparison of predicted scattering amplitude with experimentally measured result (Horne 1983): —, analysis, \circ , experiment.

20.3 cm. The velocity field of the vortex was assumed two-dimensional and inferred from static pressure measurements at the disk surface.

The experiments indicate that the amplitude of the scattered field varies linearly with the circulation of the vortex and inversely with the wavelength of the incident waves, as predicted by (44) and by the various theories mentioned above, and in agreement with the present numerical computations and those of Candel (1979). Figure 22 shows the amplitude of the experimentally measured scattered wave, for a vortex circulation of $2.7 \text{ m}^2 \text{ s}^{-1}$, and an incident frequency of 5000 Hz. This gives a value of $\Gamma/(a_\infty \lambda)$ of 0.12, and is thus in the range where the first-order approximation, (44), should apply. The value of r/λ is about 3. The location of the maximum tangential velocity is not known from the experiments, but is approximately the location of the tangential air jets. This gives a value of \tilde{r}_0 of 9.0. Qualitatively, the amplitude of the scattered waves shown in figure 22 is similar to the computational result and the analytical theory. Scattering is peaked at about $\pm 35^\circ$, which is near the value predicted by the computations, $\pm 30^\circ$ at a comparable value of r/λ . The scattering is close to zero in the forward direction. The measured back scattering is somewhat larger than the computations, but since the radius of the traverse arc is greater than the radius where the sound source is located, measurements at angles far from the forward direction are not reliable, since the incident sound field is not planar in those regions (Horne 1983). Also plotted in figure 22 is the analytical result for $\tilde{r}_0 = 9$ at $r/\lambda = 3$. The location of the peak scattering is well predicted by the analysis. The peak scattering level is underpredicted by about 50%. Such a numerical agreement is probably fortuitous in the light of the approximate nature of the value for \tilde{r}_0 from the experiments, three-dimensional effects present in the experiments, and the relatively close proximity of the plane wave source to the vortex core. The main point is that there is a good *qualitative* similarity between the computed results, the analysis, and the experiments.

6. Summary

The scattering of sound waves by a compressible vortex in the low-frequency limit has been studied using direct computation with the Navier–Stokes equations, analytically with asymptotic expansions when the wavelength of the incident sound is long, and with a high-frequency ray-tracing computation.

The accuracy of the numerical computations is verified by comparing the results for zero-circulation vortices to the results predicted by an acoustic analogy. The excellent agreement between the two results computed in fundamentally different ways indicates that numerical discretization did not act as a source of sound in the computations, and that an accurate acoustic field can be computed along with a hydrodynamic field whose amplitude is five orders of magnitude larger. We assert that such computations, however, require highly accurate differentiation and time-marching schemes, and effective non-reflecting boundary conditions. The accuracy of the boundary conditions used for the present computations was verified by ensuring that the scattering computed on different-sized computational domains converged to the same result.

The Navier–Stokes solutions, the long-wavelength analytical solution, the high-frequency solution, and the experiments of Horne (1983) all give essentially the same picture of the scattering from the finite-circulation vortex. Since the tangential velocity of the vortex decays slowly, as $1/r$ for large r , solutions from acoustic analogies proposed by many investigators fail to capture the correct directivity and scaling with r of the scattered field, owing to the slow decay of the source terms, and/or neglecting of terms that relate to long-range refraction effects. The current results show that the scattered wave amplitude is greatest in the forward scattering direction, where it is peaked in bands on either side of the forward direction. The scattered field directivity is symmetric about $\theta = 0$ for small values of the parameter $\Gamma/(a_\infty \lambda)$. The angle where the maximum occurs is found to decrease with increasing distance from the vortex core, going to zero as $r \rightarrow \infty$. When the incident waves are generated far from the core, the peak scattering level becomes constant with r away from the forward direction, in both the long-wavelength analytical solutions and by the high-frequency ray tracing. In the long-wavelength approximation, where the incident waves are only assumed planar as their distance from the core approaches infinity, the scattering amplitude is singular in the forward direction, indicating that the waves are refracted very significantly by the flow field in that direction.

The computations and analysis for the circulating-vortex case lead us to assert that direct computations, which resolve both the near-field hydrodynamic sources and the far-field sound, are an effective means with which to verify the accuracy and robustness of various acoustic analogy approaches. In flows of practical interest such as those involving jets, mixing layers, wakes and boundary layers the flow field is not compact, and, as in vortex scattering, the rearrangement of the equations leading to differentiation of acoustic sources from wave propagation and refraction effects is ambiguous. Direct computations, in addition to experimental evidence when available, provide a means of removing the ambiguity by evaluating any proposed rearrangements and the associated acoustic analogies.

The authors are indebted to Professor J. B. Keller for suggesting the high-frequency analysis and for his assistance in carrying it out. The authors would also like to thank Dr Cliff Horne for bringing his experiments to their attention and for his helpful discussions, and Dr M. E. Goldstein for his helpful remarks. This work was supported by the Office of Naval Research under contract numbers ONR-N00014-88-K-0592 and ONR-N00014-92-J-1626. The computer time was provided by NASA-Ames Research Center. Some of this work was presented in *AIAA Paper-91-0494*.

Appendix. High-frequency approximation for the refraction of plane waves in the finite-circulation vortex

In the limit where the frequency of the incident waves is large, the high-frequency, or geometrical-acoustics, approximation can be used. Starting with the Euler equations in Cartesian coordinates:

$$\rho(u_t + uu_x + vv_y) + p_x = 0, \quad (\text{A } 1a)$$

$$\rho(v_t + uv_x + vv_y) + p_y = 0, \quad (\text{A } 1b)$$

$$\rho_t + u\rho_x + v\rho_y + \rho(u_x + v_y) = 0, \quad (\text{A } 1c)$$

$$s_t + us_x + vs_y = 0, \quad (\text{A } 1d)$$

$$s = s(p, \rho), \quad (\text{A } 1e)$$

where the subscripts indicate differentiation. Now, linearizing about (time-invariant) vortex flow, $(\bar{u}, \bar{v}, \bar{\rho}, \bar{p})$, and noting that $\bar{s} = 0$, we obtain

$$u'_t + \bar{u}u'_x + \bar{v}v'_y + (1/\bar{\rho})p'_x + u'\bar{u}_x + v'\bar{u}_y + (\rho'/\bar{\rho})(\bar{u}u'_x + \bar{v}v'_y) = 0, \quad (\text{A } 2a)$$

$$v'_t + \bar{u}v'_x + \bar{v}v'_y + (1/\bar{\rho})p'_y + u'\bar{v}_x + v'\bar{v}_y + (\rho'/\bar{\rho})(\bar{u}v'_x + \bar{v}v'_y) = 0, \quad (\text{A } 2b)$$

$$\rho'_t + \bar{u}\rho'_x + \bar{v}\rho'_y + \bar{\rho}(u'_x + v'_y) + \rho'(\bar{u}_x + \bar{v}_y) + u'\bar{\rho}_x + v'\bar{\rho}_y = 0, \quad (\text{A } 2c)$$

$$s'_t + \bar{u}s'_x + \bar{v}s'_y = 0, \quad (\text{A } 2d)$$

$$s' = (1/\bar{p})(p' - \bar{a}^2\rho'). \quad (\text{A } 2e)$$

Now a solution of the form

$$u' = e^{-i\omega t} U(x, y) e^{i\omega\phi(x, y)}, \quad v' = e^{-i\omega t} V(x, y) e^{i\omega\phi(x, y)}, \quad (\text{A } 3a, b)$$

$$\rho' = e^{-i\omega t} R(x, y) e^{i\omega\phi(x, y)}, \quad p' = e^{-i\omega t} P(x, y) e^{i\omega\phi(x, y)}, \quad (\text{A } 3c, d)$$

$$s' = e^{-i\omega t} S(x, y) e^{i\omega\phi(x, y)} \quad (\text{A } 3e)$$

is assumed. Inserting (A 3) into (A 2) and retaining the terms of highest order in ω gives

$$(\bar{u}\phi_x + \bar{v}\phi_y - 1)U + (\bar{p}\phi_x/\bar{\rho})S + (\bar{a}^2\phi_x/\bar{\rho})R = 0, \quad (\text{A } 4a)$$

$$(\bar{u}\phi_x + \bar{v}\phi_y - 1)V + (\bar{p}\phi_y/\bar{\rho})S + (\bar{a}^2\phi_y/\bar{\rho})R = 0, \quad (\text{A } 4b)$$

$$(\bar{u}\phi_x + \bar{v}\phi_y - 1)R + \bar{\rho}\phi_x U + \bar{\rho}\phi_y V = 0, \quad (\text{A } 4c)$$

$$(\bar{u}\phi_x + \bar{v}\phi_y - 1)S = 0. \quad (\text{A } 4d)$$

In order for a solution to (A 4) to exist, the determinant of the system must be equal to zero. Enforcing this condition yields

$$(\bar{u}f + \bar{v}g - 1)^2 ((\bar{u}f + \bar{v}g - 1)^2 - \bar{a}^2(f^2 + g^2)) = 0, \quad (\text{A } 5)$$

where $f = \phi_x$ and $g = \phi_y$. Note that the solution $\bar{u}f + \bar{v}g - 1 = 0$ does not correspond to an acoustic wave, but to a convecting disturbance. Therefore we must have $\bar{u}f + \bar{v}g - 1 \neq 0$, which implies that $S = 0$ from (A 4d). To solve (A 5), we use the method of characteristics. Let z parameterize the characteristic curves. Their trajectories $(x(z), y(z))$, and phase function $\phi(z)$ are given by the solution of

$$\dot{x} = 2(\bar{u}f + \bar{v}g - 1)\bar{u} - 2\bar{a}^2f, \quad \dot{y} = 2(\bar{u}f + \bar{v}g - 1)\bar{v} - 2\bar{a}^2g, \quad (\text{A } 6a, b)$$

$$\dot{f} = -2(\bar{u}f + \bar{v}g - 1)(\bar{u}_x f + \bar{v}_x g) + \bar{a}_x^2(f^2 + g^2), \quad (\text{A } 6c)$$

$$\dot{g} = -2(\bar{u}f + \bar{v}g - 1)(\bar{u}_y f + \bar{v}_y g) + \bar{a}_y^2(f^2 + g^2), \quad (\text{A } 6d)$$

$$\dot{\phi} = -2(\bar{u}f + \bar{v}g - 1), \quad (\text{A } 6e)$$

where the dot indicates differentiation with respect to z .

To determine the amplitude of the wave along each ray, say the density amplitude, the terms of next highest order in ω must be retained in (A 2). We need only solve for one of R , U , or V , since each can be written as a function of only one of them by solving the system of equations (A 4) once the phase function is determined. Carrying out the algebra gives, for the density amplitude function,

$$\dot{R} = 2R((2\bar{a}^2/\phi)(f(\bar{u}f + \bar{v}g)_x + g(\bar{u}f + \bar{v}g)_y) - (\bar{a}^2f)_x - (\bar{a}^2g)_y + (\bar{u}_x + \bar{v}_y)), \quad (\text{A } 7)$$

where (A 6) have been used to simplify the final result. Equation (A 7) can be integrated in z along with (A 6) to give the desired solution. However, the terms f_x , f_y , g_x and g_y in (A 7) cannot be found from the solutions to (A 6) alone, since we only know the derivatives of the functions f and g along the rays. One way of overcoming this difficulty is to integrate additional equations for derivatives of f and g normal to the ray paths, thus providing the information to determine their derivatives in any direction. Let α denote the direction normal to the plane waves at $z = 0$, the initial location of the plane incident wave. The following equations can be found by differentiating (A 6) with respect to α . First rewrite A 6(a-d) using vector notation:

$$\dot{X} = F(X), \quad (\text{A } 8)$$

where $X = (x, y, f, g)$, and F is a vector function whose individual elements are given by the right-hand sides of (A 6). Differentiating with respect to α gives

$$\dot{X}_\alpha = \frac{\partial F}{\partial X} \cdot X_\alpha, \quad (\text{A } 9)$$

Now there are ten ordinary differential equations in all to integrate in z . The initial conditions corresponding to a plane wave at some distance $-x_0$ from the vortex core are

$$x(0) = -x_0, \quad y(0) = \alpha, \quad f(0) = 1, \quad g(0) = 0, \quad (\text{A } 10 a-d)$$

$$\phi(0) = 0, \quad R(0) = 1, \quad (\text{A } 10 e, f)$$

where the amplitude is normalized by the amplitude of the plane wave, and

$$x_\alpha(0) = 0, \quad y_\alpha(0) = 1, \quad f_\alpha(0) = 0, \quad g_\alpha(0) = 0. \quad (\text{A } 10 g-j)$$

The equations are advanced using a fourth-order Runge-Kutta scheme with adaptive step size. The step size is modified to attempt to keep the local error in the solution from exceeding one part in 1000. The vortex flow field, $(\bar{u}, \bar{v}, \bar{\rho}, \bar{p})$, is given by (3)–(7) in §2. The solution for the rays that form the caustic is modified to integrate across the singularity exactly, and correct the amplitude by the factor of i . The program was checked by comparing the ray trajectories with those found by Georges (1972), which were identical. The results of several runs can be found in §4.

REFERENCES

- ABRAMOWITZ, M. A. & STEGUN, I. A. 1972 *Handbook of Mathematical Functions*. Dover.
 BROADBENT, E. G. & MOORE, D. W. 1979 Acoustic destabilization of vortices. *Phil. Trans. R. Soc. Lond. A* **290**, 353–371.
 CANDEL, S. M. 1979 Numerical solution of wave scattering problems in the parabolic approximation. *J. Fluid. Mech.* **90**, 465–507.
 COLONIUS, T., LELE, S. K. & MOIN, P. 1991a Scattering of sound waves by a compressible vortex. *AIAA Paper* 91-0494.
 COLONIUS, T., LELE, S. K. & MOIN, P. 1991b The free compressible viscous vortex. *J. Fluid. Mech.* **230**, 45–73.

- COLONIUS, T., LELE, S. K. & MOIN, P. 1992 Boundary conditions for direct computation of aerodynamic sound. *AIAA J.* **31**, 1574–1582.
- CRIGHTON, D. G. 1975 Basic principles of aerodynamic noise generation. *Prog. Aerospace Sci.* **16**, 31–96.
- CRIGHTON, D. G. 1988 Goals for computational aeroacoustics. In *Computational Acoustics: Algorithms and Applications* (ed. D. Lee, R. L. Sternberg & M. H. Schultz). Elsevier.
- FERZIGER, J. H. 1974 Low-frequency acoustic scattering from a trailing vortex. *J. Acoust. Soc. Am.* **56**, 1705–1707.
- GEORGES, T. M. 1972 Acoustic ray paths through a model vortex with a viscous core. *J. Acoust. Soc. Am.* **51**, 206–209.
- GILES, M. B. 1990 Non-reflecting boundary conditions for Euler equation calculations. *AIAA J.* **12**, 2050–2058.
- HORNE, W. C. 1983 Measurements of the scattering of sound by a line vortex. *AIAA Paper* 83-0676.
- HOWE, M. S. 1975 Contributions to the theory of aerodynamic sound, with application to excess jet noise and the theory of the flute. *J. Fluid. Mech.* **71**, 625–673.
- LELE, S. K. 1992 Compact finite difference schemes with spectral-like resolution. *J. Comput. Phys.* **103**, 16–42.
- LIGHTHILL, M. J. 1952 On sound generated aerodynamically. *Proc. R. Soc. Lond. A* **211**, 564–587.
- MÜLLER, E. A. & MATSCHAT, K. R. 1959 The scattering of sound by a single vortex and by turbulence. *Tech. Rep. Max-Planck-Inst. für Strömungsforschung, Göttingen*.
- O'SHEA, S. 1975 Sound scattering by a potential vortex. *J. Sound Vib.* **43**, 109–116.
- TANAKA, K. & ISHII, S. 1981 Scattering of a plane sound wave by a vortex pair. *J. Phys. Soc. Japan* **51**, 1992–1999.
- TAYLOR, G. I. 1918 On the dissipation of eddies. *Aero. Res. Comm., R and M* 598.
- YATES, J. E. 1978 Application of the Bernoulli enthalpy concept to the study of vortex noise and jet impingement noise. *NASA Contractor Rep.* 2987.